Journal of the Mechanics and Physics of Solids 142 (2020) 104045

Contents lists available at ScienceDirect

Journal of the Mechanics and Physics of Solids

journal homepage: www.elsevier.com/locate/jmps

Hard-magnetic elastica

Liu Wang[a,b,1], Yoonho Kim[a,1], Chuan Fei Guo[b,c], Xuanhe Zhao[a,d,*]

[a] Department of Mechanical Engineering, Massachusetts Institute of Technology, Cambridge, MA 02139, USA
[b] Department of Materials Science and Engineering, Southern University of Science and Technology, Shenzhen 518055, China
[c] Shenzhen Engineering Research Center for Novel Electronic Information Materials and Devices, Southern University of Science and Technology, Shenzhen 518055, China
[d] Department of Civil and Environmental Engineering, Massachusetts Institute of Technology, Cambridge, MA 02139, USA

ARTICLE INFO

Article history:
Received 14 December 2019
Revised 2 May 2020
Accepted 29 May 2020
Available online 2 June 2020

ABSTRACT

Recently, *ferromagnetic soft continuum robots* – a type of slender, thread-like robots that can be steered magnetically – have demonstrated the capability to navigate through the brain's narrow and winding vasculature, offering a range of captivating applications such as robotic endovascular neurosurgery. Composed of soft polymers with embedded hard-magnetic particles as distributed actuation sources, ferromagnetic soft continuum robots produce large-scale elastic deflections through magnetic torques and/or forces generated from the intrinsic magnetic dipoles under the influence of external magnetic fields. This unique actuation mechanism based on distributed intrinsic dipoles yields better steering and navigational capabilities at much smaller scales, which differentiate them from previously developed continuum robots. To account for the presence of intrinsic magnetic polarities, this emerging class of magnetic continuum robots provides a new type of active structure – *hard-magnetic elastica* – which means a thin, elastic strip or rod with hard-magnetic properties. In this work, we present a nonlinear theory for hard-magnetic elastica, which allows accurate prediction of large deflections induced by the magnetic body torque and force in the presence of an external magnetic field. From our model, explicit analytical solutions can be readily obtained when the applied magnetic field is spatially uniform. Our model is validated by comparing the obtained solutions with both experimental results and finite element simulations. The validated model is then used to calculate required magnetic fields for the robot's end tip to reach a target point in space, which essentially is an inverse problem challenging to solve with a linear theory or finite-element simulation. Providing facile routes to analyze nonlinear behavior of hard-magnetic elastica, the presented theory can be used to guide the design and control of the emerging class of magnetically steerable soft continuum robots.

1. Introduction

Unlike conventional robots with discrete joints, continuum robots produce motion through the generation of smooth curves via large scale elastic deformation, similar to the tentacles or tongues of animals (Camarillo et al., 2009; Dalvand et al., 2018; Edelmann et al., 2017; Renda et al., 2012; Robinson and Davies, 1999) and hence can be applied to important

---

[*] Corresponding author.
E-mail address: zhaox@mit.edu (X. Zhao).

[1] These authors contributed equally to the current work.

https://doi.org/10.1016/j.jmps.2020.104045

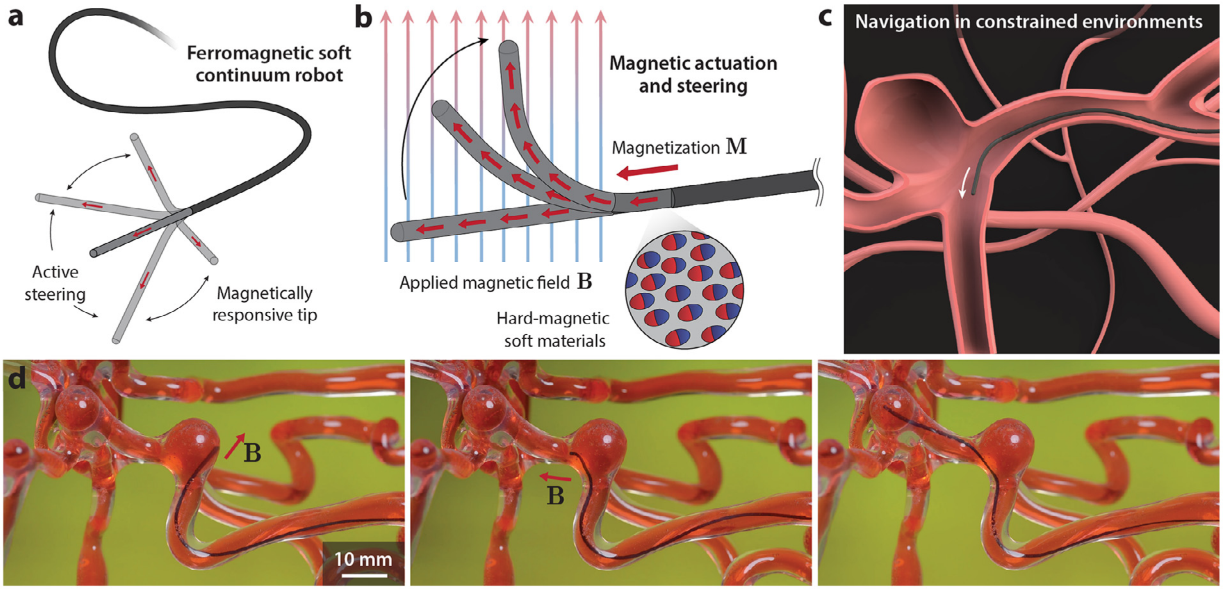

Fig. 1. (**a**) Schematic of the ferromagnetic soft continuum robot with a magnetically responsive tip. (**b**) Schematic of the magnetically responsive tip with programmed uniform magnetization **M** resulting from the hard-magnetic particles embedded in the robot's body made of a soft polymer matrix. **(c)** Illustration of the active steerability of the ferromagnetic soft continuum robot navigating in a complex neurovasculature with an aneurysm. **(d)** Experimental demonstration (Kim et al., 2019) of the ferromagnetic soft continuum robot navigating in a 3D cerebrovascular phantom network. Adapted from Ref Kim et al. (2019).

medical applications such as minimally invasive surgery (Fu et al., 2009; Menaker et al., 2018; Runciman et al., 2019). Despite the ability to carry out tasks under remote control, existing continuum robots have demonstrated limited practical utility, mainly because of miniaturization challenges inherent in their conventional actuation mechanisms based on pulling mechanical wires or inflating pneumatic or hydraulic chambers (Clogenson et al., 2014; Ranzani et al., 2015; Shepherd et al., 2011). Recent work by Kim et al., 2019 aiming at tackling these challenges has developed sub-millimeter-scale, soft-bodied, and magnetically steerable continuum robots – so-called *ferromagnetic soft continuum robots* (**Fig. 1a**) – which were enabled by the use of hard-magnetic (*e.g.,* NdFeB) particles that are uniformly dispersed throughout the robot's body as distributed actuation sources. These embedded hard-magnetic particles, which are intrinsic dipoles once magnetized, generate magnetic torques and/or forces when external magnetic fields are applied for actuation (Lum et al., 2016; Kim et al., 2018; Zhao et al., 2019). The generated magnetic torques and forces collectively lead to large scale elastic deflections of the robot's body, as the intrinsic dipoles reorient themselves along the applied field direction (**Fig. 1b**). This unique actuation mechanism yields better steering capabilities at much smaller scales than conventional continuum robots, thereby enabling navigation in tight spaces such as the brain's vasculature (**Fig. 1c**). Based on these capabilities, the work has demonstrated navigating in a life-sized silicone replica of the brain's blood vessels with ferromagnetic soft continuum robots under remotely applied magnetic fields (**Fig. 1d**). In addition to the soft continuum robots, hard-magnetic materials have also been utilized for fabricating other types of soft robots such as microswimmers (Diller et al., 2014; Hu et al., 2018; Zhang and Diller, 2018).

To analyze this emerging class of magnetically steerable soft continuum robots, a suitable theoretical model to accurately describe their nonlinear magnetoelastic behavior is warranted. Although a general, continuum-level framework for computational analysis of so-called *hard-magnetic soft materials* was presented by Zhao et al. (2019), such computational analysis with finite element simulation is of limited use in practice because of their high computational cost. More importantly, such numerical approaches in finite element environments are not favorable to solving inverse problems, where calculation of required magnetic fields to achieve desired configuration of the robot is of greater importance than simply predicting the robot's behavior under specified input fields. To facilitate the use of analytical solutions, as well as the insights provided by them, in the design and control of ferromagnetic soft continuum robots, we formulate a new type of problems – so-called *hard-magnetic elastica* – which deals with the large scale deflection of an elastic rod made of a homogenous continuum of hard-magnetic soft materials.

Despite the long and checkered history underlying the elastica theory, systematic analyses of hard-magnetic elastica have remained largely unexplored. This is mainly because previous studies of magnetoactive elastica were mostly focused on elastic beams or rods composed of soft-magnetic (*e.g.,* carbonyl iron) materials (Ciambella et al., 2018; Danas et al., 2012; Schmauch et al., 2017; Singh and Onck, 2018) or paramagnetic materials (Gerbal et al., 2015). As illustrated in **Fig. 2a**, paramagnetic materials do not retain any remanent magnetization, and their magnetization is highly dependent on the externally

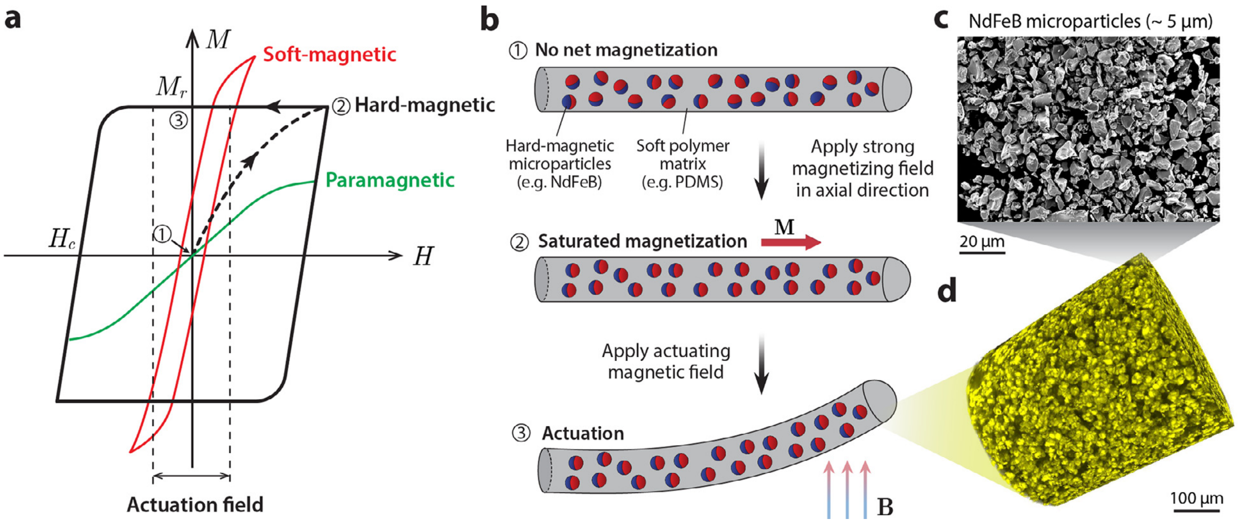

Fig 2. **(a)** Magnetization curves and hysteresis loops of hard-magnetic (black), soft-magnetic (red), and paramagnetic (green) materials. The curves show the magnetization (M) as a function of the applied magnetic field strength (H). Hard-magnetic materials maintain the remanent magnetization (M_r) when the actuation field strength is much smaller than the coercivity (H_c). **(b)** Schematic illustration of the hard-magnetic elastica with programmed remanent magnetization resulting from the aligned hard-magnetic particles with intrinsic dioples in the polymer matrix. **(c)** Scanning electron microscope (SEM) image of NdFeB microparticles with an average size of around 5 μm. (d) Micro computerized tomography (µCT) image of NdFeB microparticles uniformly distributed in the PDMS matrix (20 vol%).

applied magnetic field. While soft-magnetic materials can possess remanent magnetization, it can be easily reverted by external magnetic fields because of their relatively low coercivity, which is comparable with the applied field for actuation. On the contrary, hard-magnetic materials, once magnetically saturated, have relatively high coercivity and hence can retain remanent magnetization (denoted as M_r in Fig. 2**a**) as long as the applied actuating magnetic field is sufficiently lower than the coercivity (denoted as H_c in Fig. 2**a**). Within this range of actuating fields far below the coercivity (Fig. 2**a**), it is reasonable to assume that the remanent magnetization of hard-magnetic materials remains unaffected by the externally applied magnetic field.

Typical composition and microstructure of the hard-magnetic elastica are illustrated in Fig. 2**b**. Magnetically isotropic hard-magnetic microparticles (*e.g.*, NdFeB with average size of 5 μm in Fig. 2**c**) are uniformly dispersed within a soft polymer matrix (*e.g.*, PDMS in Fig. 2**d**). Upon fabrication into a slender rod through either injection molding or printing (Kim et al., 2019), the embedded hard-magnetic particles are randomly oriented, yielding no net magnetization along the rod (*i.e.*, no net magnetization state in Fig. 2**b**). When the rod is exposed to a strong magnetic field (~2.7 T), the embedded hard-magnetic particles are magnetically saturated into one direction, which gives rise to the overall magnetic polarity along the axial direction (*i.e.*, saturated magnetization state in Fig. 2**b**). Under an actuating magnetic field (far below the coercive field), the body deforms as the embedded magnetic dipoles align themselves along the applied field direction (*i.e.*, actuation state in Fig. 2**b**).

Here, we present a theory for hard-magnetic elastica, which allows for accurate prediction of the large deflection induced by magnetic body torques and/or forces in the presence of external magnetic fields. In Section 2, we first provide a general, continuum framework for hard-magnetic soft materials including kinematic relations and constitutive equations obtained from elastic and magnetic potential energies. Then, we apply certain constraints specific to the slender geometry and planar motion of the elastica to derive the governing equations for hard-magnetic elastica in several forms. From the governing equation, we obtain explicit analytical solutions for the hard-magnetic elastica under spatially uniform magnetic fields. In Section 3, we also present deformed configurations of the hard-magnetic elastica calculated while varying the orientation of the applied magnetic field with respect to the magnetization direction of the elastica. For two specific cases, as illustrative examples, in which the actuating magnetic field is applied in the direction either perpendicular or antiparallel to the residual magnetization of the hard-magnetic elastica, we validate our model by comparing the obtained solutions with both experimental results and finite element simulations presented by Zhao et al. (2019) in Section 4. Extending the validated model to specific applications relevant to the ferromagnetic soft continuum robots, in Section 5, we construct a plot visualizing the full workspace by the end-effector of the robot in space under a varying magnetic field, which in turn can be used to control the navigation of the robot. We conclude in **Section 6** where we also speculate on the potential use of the developed framework for hard-magnetic elastica in the design and control of the emerging class of ferromagnetic soft continuum robots.

2. Theory

2.1. General continuum framework and constitutive relations

We begin by describing a general, continuum-level framework with kinematic relations for hard-magnetic soft materials, which we consider as a homogenized continuum that constitutes a deformable, elastic solid with hard-magnetic properties. The underlying assumption in the analysis of hard-magnetic soft materials is that, once the intrinsic magnetic dipoles are magnetically saturated, the residual magnetization density can be considered an independent variable, which remains unaffected by the applied actuating field unless it exceeds the coercivity of the embedded hard-magnetic material. Moreover, because the permeability of the fully saturated hard-magnetic particles and polymer matrix (relative permeability of 1.04 and 1.00, respectively) used in the current study is approximately the same as that of air, the presence of the hard-magnetic elastica will not perturb the applied actuation magnetic field (Pyrhönen et al., 2014; Zhou and Wang, 2016). Therefore, the magneto-mechanical coupling in the hard-magnetic elastica arises only from the deformation-induced variation of the remanent magnetization (*e.g.,* rotation of the remanent magnetization vector) in the applied magnetic field. Provided that the actuating magnetic field is in general far below the coercivity, we can consider a mechanically soft, deformable body with permanent magnetization density. Any material point in the solid of interest is identified by its initial position vector $\mathbf{X}$ in the reference (undeformed) configuration, while the same material point in the deformed (current) configuration is given by $\mathbf{x} = \chi(\mathbf{X})$, where the mapping χ describes the deformation of the body. The deformation gradient tensor $\mathbf{F}$ is defined as

$$\mathbf{F} = \mathrm{Grad}\,\chi, \tag{1}$$

where Grad denotes the material gradient with respect to $\mathbf{X}$ in the reference configuration. The volumetric Jacobian is defined as $J = \det\mathbf{F} > 0$, which characterizes the change in material volume elements during the deformation.

The magnetization density is denoted by a vector $\mathbf{M}$ in the reference configuration and $\mathbf{m}$ in the deformed configuration. Likewise, the magnetic charge density, a scalar quantity, is denoted by ρ_M and ρ_m in the reference and deformed configurations, respectively. The conservation of total magnetic charge requires $\rho_M = J\rho_m$, which can be written in terms of the magnetization density in a differential form as

$$\mathrm{Div}\mathbf{M} = J\mathrm{div}\mathbf{m}, \tag{2}$$

where Div denotes the material divergence with respect to $\mathbf{X}$ in the reference configuration, while div denotes the spatial divergence with respect to $\mathbf{x}$ in the deformed configuration. It is worth noting that 1) the magnetic charge density is analogous to the polarization charge density in electrostatics, except that a magnetic monopole has never been observed, and 2) the magnetization density can be spatially nonuniform, which leads to a nonzero magnetic charge density. Combining the divergence theorem with the Nanson's formula, which characterizes the area change, we obtain the following kinematic relation for the divergence of any vector field $\mathbf{A}$:

$$\mathrm{Div}\mathbf{A} = J\mathrm{div}(J^{-1}\mathbf{F}\mathbf{A}). \tag{3}$$

From Eqs. (2) and (3) we obtain the relation between $\mathbf{M}$ and $\mathbf{m}$ as

$$\mathbf{m} = J^{-1}\mathbf{F}\mathbf{M}. \tag{4}$$

Under isothermal conditions, work done by the externally applied magnetic field $\mathbf{B}$ is stored as Helmholtz free energy, which can be expressed per unit current volume as

$$\psi^{\mathrm{magnetic}} = -\mathbf{m}\cdot\mathbf{B}, \tag{5}$$

and per unit reference volume in terms of the referential magnetization density $\mathbf{M}$ as

$$\psi_{\mathrm{R}}^{\mathrm{magnetic}}(\mathbf{F}) = J\psi^{\mathrm{magnetic}} = -\mathbf{F}\mathbf{M}\cdot\mathbf{B}, \tag{6}$$

which becomes a function of the deformation gradient $\mathbf{F}$. The elastic part of the Helmholtz free energy – also known as strain energy – per unit reference volume is also a function of the deformation gradient: $\psi_{\mathrm{R}}^{\mathrm{elastic}}(\mathbf{F})$. For this strain energy function, several specific forms and constitutive laws to describe the elastic properties of materials are available: neo-Hookean, Mooney-Rivlin, Ogden, Arruda-Boyce, and so on. The total Helmholtz free energy density is the sum of the elastic and magnetic components: $\psi_{\mathrm{R}}(\mathbf{F}) = \psi_{\mathrm{R}}^{\mathrm{elastic}}(\mathbf{F}) + \psi_{\mathrm{R}}^{\mathrm{magnetic}}(\mathbf{F})$.

For isothermal processes, the dissipation inequality reads that the rate of change in the free energy stored in the body is less than, or at most equal to, the power expended on the body:

$$\mathcal{D}_{\mathrm{int}} = \mathbf{P} : \dot{\mathbf{F}} - \dot{\psi}_{\mathrm{R}} \geq 0. \tag{7}$$

Here, $\mathcal{D}_{\mathrm{int}}$ denotes the internal dissipation, $\mathbf{P} : \dot{\mathbf{F}}$ denotes the rate of internal mechanical work, where $\mathbf{P}$ is the first Piola-Kirchhoff stress tensor (or nominal stress) which forms a work conjugate pair with the time derivative of the deformation gradient $\dot{\mathbf{F}}$, and $\dot{\psi}_{\mathrm{R}}$ is the rate of change in the total Helmholtz free energy. For hyperelastic materials, from the inequality (7) with the chain rule, the Piola stress is obtained from the derivative of the free energy function with respect to $\mathbf{F}$:

$$\mathbf{P} = \frac{\partial\psi_{\mathrm{R}}}{\partial\mathbf{F}}. \tag{8}$$

Then, by definition, the Cauchy (or true) stress tensor is expressed as

$$\boldsymbol{\sigma} = J^{-1} \frac{\partial \psi_{\mathrm{R}}}{\partial \mathbf{F}} \mathbf{F}^{\mathrm{T}}, \tag{9}$$

where $\mathbf{F}^{\mathrm{T}}$ denotes the transpose of the deformation gradient tensor. From Eqs. (6) and (9), the magnetic Cauchy stress can be expressed as

$$\boldsymbol{\sigma}^{\text{magnetic}} = -J^{-1}\mathbf{B} \otimes \mathbf{FM} = -\mathbf{B} \otimes \mathbf{m}, \tag{10}$$

where the operator $\otimes$ denotes the dyadic product that takes two vectors to yield a second-order tensor. The application of an actuating magnetic field $\mathbf{B}$ to the intrinsic magnetic dipoles in the material generates the magnetic Cauchy stress. The magnetic Cauchy stress drives the deformation of the material, which leads to the elastic Cauchy stress, denoted by $\boldsymbol{\sigma}^{\text{elastic}}$. The total Cauchy stress is then expressed as:

$$\boldsymbol{\sigma} = \boldsymbol{\sigma}^{\text{elastic}} + \boldsymbol{\sigma}^{\text{magnetic}} = J^{-1} \frac{\partial \psi_{\mathrm{R}}^{\text{elastic}}(\mathbf{F})}{\partial \mathbf{F}} \mathbf{F}^{\mathrm{T}} - J^{-1}\mathbf{B} \otimes \mathbf{FM}. \tag{11}$$

Assuming quasi-static conditions, the following equation of linear momentum balance must be satisfied everywhere in the deformed body for the material to be in equilibrium:

$$\operatorname{div}\boldsymbol{\sigma} + \mathbf{b} = \mathbf{0}, \tag{12}$$

where $\mathbf{b}$ denotes the body force per unit current volume. This equilibrium equation can be solved for the deformation gradient $\mathbf{F}$ to find the equilibrium configuration of the given hard-magnetic soft material under magnetic actuation. This continuum-level approach based on elastic and magnetic Cauchy stresses is particularly useful in finite element environments when the given geometry is complicated, as demonstrated in previous studies by Kim et al. (2018), Zhao et al. (2019), because the constitutive equations can be readily implemented in commercial finite element software packages such as Abaqus.

When the magnetic Cauchy stress is employed in the analysis of hard-magnetic soft materials, the magnetic body torque and force are automatically taken into account via suitable mechanical balance laws. From the angular momentum balance, for example, the magnetic body torque (per unit current volume) can be expressed in terms of the magnetic Cauchy stress as

$$\boldsymbol{\tau}^{\text{magnetic}} = -\boldsymbol{\mathcal{E}} : \left(\boldsymbol{\sigma}^{\text{magnetic}}\right)^{\mathrm{T}} = \mathbf{m} \times \mathbf{B} = J^{-1}\mathbf{FM} \times \mathbf{B}, \tag{13}$$

where $\boldsymbol{\mathcal{E}} = \varepsilon_{ijk}\mathbf{e}_i \otimes \mathbf{e}_j \otimes \mathbf{e}_k$ is the third-order permutation tensor, and the operator $:$ denotes the double contraction of two tensors. If the magnetization density is spatially uniform across the material, from the linear momentum balance in Eq. (12), the magnetic body force (per unit current volume) can be expressed in terms of the magnetic Cauchy stress as

$$\mathbf{b}^{\text{magnetic}} = -\operatorname{div}\boldsymbol{\sigma}^{\text{magnetic}} = \operatorname{div}(\mathbf{B} \otimes \mathbf{m}) = (\operatorname{grad}\mathbf{B})\mathbf{m} = J^{-1}(\operatorname{grad}\mathbf{B})\mathbf{FM}, \tag{14}$$

where grad denotes the spatial gradient with respect to $\mathbf{x}$ in the deformed configuration. From Eq. (14) we know that, when the applied magnetic field $\mathbf{B}$ is spatially uniform, the magnetic body force term vanishes, and therefore the actuation of hard-magnetic soft materials is driven by the magnetic torque. Equivalently, the magnetic body force (per unit volume) can also be expressed as the negative gradient of the magnetic potential energy defined in Eq. (5) as

$$\mathbf{b}^{\text{magnetic}} = -\operatorname{grad}\psi^{\text{magnetic}} = (\operatorname{grad}\mathbf{B})^{\mathrm{T}}\mathbf{m} = J^{-1}(\operatorname{grad}\mathbf{B})^{\mathrm{T}}\mathbf{FM}. \tag{15}$$

Note that, for irrotational (curl-free) magnetic fields with no free current, the spatial gradient is symmetric: $\operatorname{grad}\mathbf{B} = (\operatorname{grad}\mathbf{B})^{\mathrm{T}}$, which makes the two expressions in Eqs. (14) and (15) identical.

It is worth noting that the magnetic body torque generated by the embedded magnetized particles under external magnetic fields causes the magnetic Cauchy stress in Eq. (10) to be asymmetric. Correspondingly, in the presence of magnetic body torques, the total Cauchy stress in Eq. (11) can also be asymmetric. It should also be noted that for conventional isotropic magnetorheological elastomers with soft-magnetic inclusions, whrere no body torque or couple stress exists, the Cauchy stress should remain symmetric to satisfy the angular momentum balance, as discussed in a large volume of literature (Dorfmann and Ogden, 2003, 2004, 2014; Holzapfel, 2001).

2.2. Hard-magnetic elastica: kinematic relations and governing equations

We now focus our attention on a thin, elastic rod with hard-magnetic properties – the hard-magnetic elastica, which produces large deflections under externally applied magnetic fields owing to the presence of intrinsic dipoles (**Fig. 3a**). Although we still confine ourselves to quasi-static problems under isothermal conditions, the transition from the general continuum framework for hard-magnetic soft materials to the analysis of hard-magnetic elastica requires a set of restrictions specific to the slender geometry and planar motion of the elastica. While more generalized rod theories (*e.g.*, Kirchhoff's, Cosserat's, Green and Naghi's) can analyze the stretching, twisting, and transverse shearing as well as the bending of rods (Bretl and McCarthy, 2013; Jiang et al., 2016; Kratchman et al., 2016; Tunay, 2013), the twisting motion has low practical implications for the interest in magnetically steerable soft continuum robots and hence can be ruled out. Plus, for a slender body with

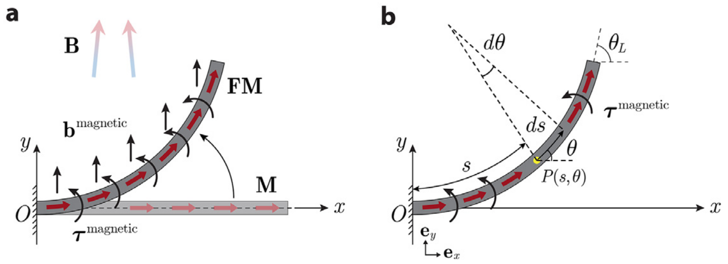

Fig. 3. **(a)** Ferromagnetic soft continuum robot deforms under the applied magnetic field **B**. Magnetization vector **M** in the reference state (shown by dim red arrows) changes to **FM** in the deformed state (shown by bright red arrows) where **F** is the deformation gradient. Symbols $\mathbf{b}^{\text{magnetic}}$ and $\boldsymbol{\tau}^{\text{magnetic}}$ denote the magnetic body force and torque density, respectively. **(b)** The geometry of the deformed robot is characterized by a parameterized spatial curve $\theta = \theta(s)$, referred to as elastica, in which s and θ represents the arc length and tangential angle at the spatial point, respectively. The rotation angle at the free-tip is denoted as θ_L.

a diameter much smaller than its length, we can assume that the cross-section remains perpendicular to the centerline of the body during deformation (*i.e.,* no transverse shearing). Furthermore, we can assume that the centerline length of the elastica remains unchanged during deformation (*i.e.,* centerline inextensibility along the length direction), which will be justified later in the discussion section. Lastly, given that most polymeric materials can sustain finite strains without noticeable volume changes, we will also assume the incompressibility of constituent materials (*i.e.,* $J = 1$), which, along with the assumption of inextensibility, implies that the cross-sectional area does not vary during magnetoelastic deflections.

With these underlying assumptions specific to the slender geometry and planar motion of the hard-magnetic elastica, the curvature of the centerline (*i.e.,* a spatial curve in the current configuration) can be expressed as

$$\kappa(s) = \frac{d\theta(s)}{ds} = \theta'(s), \tag{16}$$

where s denotes the arc length from the origin to the spatial point of interest (denoted by P in **Fig. 3b**) and $\theta(s)$ denotes the angle between the tangent to the curve at point P and the reference direction (*i.e.,* x-axis in **Fig. 3b**).

For our bendable yet inextensible, twist-free hard-magnetic elastica, the strain energy density (or the elastic Helmholtz free energy per unit current volume) includes only the bending energy, but no stretching or torsional energy. The bending energy then can be expressed as a function of the curvature: $\psi^{\text{elastic}}(\theta')$. Commonly, for a slender rod, the bending energy (per unit volume) takes the following quadratic form proposed by Euler for the inextensible elastica (O'Reilly, 2017):

$$\psi^{\text{elastic}}(\theta') = \frac{EI}{2A}\theta'^2, \tag{17}$$

where E denotes Young's modulus, I is the area moment of inertia, and A is the cross-sectional area of the hard-magnetic elastica. It is worth noting that the constitutive relation for the bending energy in Eq. (17) implies the following moment-curvature relation, also known as Euler-Bernoulli relation (de Payrebrune and O'Reilly, 2016; Tunay, 2004):

$$M_{\text{b}}(s) = EI\kappa(s), \tag{18}$$

where $M_{\text{b}}(s)$ denotes the internal bending moment. This linear relation holds only for beams or rods made of linear elastic materials for which stress and strain are linearly related by Young's modulus. Even though the hard-magnetic elastica overall exhibits large scale deflections, the local maximum strain developed on an infinitesimal segment due to local compression or stretching during the magnetoelastic bending is inherently limited to a small level. Within this limited range, the constitutive relations for the constituent hyperelastic materials can be linearized, which yields the linear moment-curvature relation in Eq. (18) and the quadratic form for the bending energy in Eq. (17).

The deformation gradient, which can be decomposed into $\mathbf{F} = \mathbf{RU}$ where $\mathbf{R}$ and $\mathbf{U}$ denote the rotation and right stretch tensors, respectively, now becomes identical to pure rotation ($\mathbf{F} = \mathbf{R}$) because of the underlying assumption of inextensibility ($\mathbf{U} = \mathbf{1}$; no stretch). Furthermore, because the motion of the elastica is planar (*e.g.,* on xy-plane in **Fig. 3b**), the rotation $\mathbf{R}$ takes the basic form for the rotation around the z-axis:

$$\mathbf{R} = \mathbf{R}_z(\theta) = \cos\theta\mathbf{e}_x \otimes \mathbf{e}_x - \sin\theta\mathbf{e}_x \otimes \mathbf{e}_y + \sin\theta\mathbf{e}_y \otimes \mathbf{e}_x + \cos\theta\mathbf{e}_y \otimes \mathbf{e}_y + \mathbf{e}_z \otimes \mathbf{e}_z \tag{19}$$

Then, from Eq. (6), The magnetic potential energy per unit current volume can be expressed as

$$\psi^{\text{magnetic}}(\theta, s) = -\mathbf{RM} \cdot \mathbf{B}, \tag{20}$$

which leads to the total Helmholtz free energy density as a function of three variables (θ, θ', s): $\psi(\theta, \theta', s) = \psi^{\text{elastic}}(\theta') + \psi^{\text{magnetic}}(\theta, s)$. Then the total Helmholtz free energy of the elastica, denoted by Π, can be expressed as:

$$\Pi[\theta(s)] = A\int_0^L \psi(\theta, \theta', s)ds, \tag{21}$$

where L denotes the length of the elastica. The equilibrium state (the deformed configuration) can be found from the principle of stationary potential energy $\delta\Pi = 0$, which yields the following differential equation also known as the Euler-Lagrange equation:

$$\frac{d}{ds}\left(\frac{\partial\psi}{\partial\theta'}\right) = \frac{\partial\psi}{\partial\theta}, \tag{22}$$

from which we obtain the following governing equation for the hard-magnetic elastica:

$$\frac{d}{ds}\left(\frac{\partial\psi^{\text{elastic}}}{\partial\theta'}\right) = \frac{\partial\psi^{\text{magnetic}}}{\partial\theta}. \tag{23}$$

Substituting the elastic and magnetic potential energy densities in Eqs. (17) and (20) into Eq. (23), we obtain

$$\frac{EI}{A}\frac{d^2\theta}{ds^2} = \frac{\partial}{\partial\theta}(-\mathbf{RM}\cdot\mathbf{B}), \tag{24}$$

where the right-hand side can be expanded by applying chain rule into

$$\frac{\partial}{\partial\theta}(-\mathbf{RM}\cdot\mathbf{B}) = -\frac{\partial\mathbf{R}}{\partial\theta}\mathbf{M}\cdot\mathbf{B} - \mathbf{RM}\cdot\left(\text{grad}\mathbf{B}\frac{\partial\mathbf{x}}{\partial\theta}\right). \tag{25}$$

Here, again, the magnetization density is assumed to be spatially uniform. Given that the derivative of a rotation tensor can be expressed in terms of a skew-symmetric tensor and its axial vector (see **Appendix A** for details), the first term on the right-hand side of Eq. (25) can be re-written as

$$\frac{\partial\mathbf{R}}{\partial\theta}\mathbf{M}\cdot\mathbf{B} = \mathbf{e}_z\cdot(\mathbf{RM}\times\mathbf{B}) = [\mathbf{RM}\times\mathbf{B}]_z, \tag{26}$$

while the second term can be rearranged as

$$\mathbf{RM}\cdot\left(\text{grad}\mathbf{B}\frac{\partial\mathbf{x}}{\partial\theta}\right) = \left((\text{grad}\mathbf{B})^{\mathrm{T}}\mathbf{RM}\right)\cdot\frac{\partial\mathbf{x}}{\partial\theta}. \tag{27}$$

Then, the governing equation in Eq. (23) can be expressed as

$$\frac{EI}{A}\frac{d^2\theta}{ds^2} + [\mathbf{RM}\times\mathbf{B}]_z + \left((\text{grad}\mathbf{B})^{\mathrm{T}}\mathbf{RM}\right)\cdot\frac{\partial\mathbf{x}}{\partial\theta} = 0, \tag{28}$$

which can be equivalently expressed in terms of the magnetic body torque and force from Eqs. (13) and (15) as

$$\frac{EI}{A}\frac{d^2\theta}{ds^2} + \mathbf{e}_z\cdot\boldsymbol{\tau}^{\text{magnetic}} + \frac{\partial\mathbf{x}}{\partial\theta}\cdot\mathbf{b}^{\text{magnetic}} = 0. \tag{29}$$

Physically, the first term in Eq. (29) can be interpreted as the variation in strain energy, while the second and third terms can be interpreted as work done by the magnetic body torque and force, respectively, per unit volume of an infinitesimal element at point P in the deformed configuration during a small variation in angle θ. Eq. (29) can also be written in terms of the scalar components as

$$\frac{EI}{A}\frac{d^2\theta}{ds^2} + \tau_z^{\text{magnetic}} - b_x^{\text{magnetic}}\int_0^s \sin\theta(\eta)d\eta + b_y^{\text{magnetic}}\int_0^s \cos\theta(\eta)d\eta = 0, \tag{30}$$

in which the following kinematic relations are employed for a clamped-free elastica:

$$\mathbf{x} = \int_0^s \cos\theta(\eta)d\eta\ \mathbf{e}_x + \int_0^s \sin\theta(\eta)d\eta\ \mathbf{e}_y, \tag{31}$$

$$\frac{\partial\mathbf{x}}{\partial\theta} = -\int_0^s \sin\theta(\eta)d\eta\ \mathbf{e}_x + \int_0^s \cos\theta(\eta)d\eta\ \mathbf{e}_y, \tag{32}$$

where η is used as a dummy variable for integration. Note that Eq. (30) obtained above is equivalent to the governing equation obtained from the force and moment balance (Lum et al., 2016).

2.3. Analytical solutions for deflections under uniform magnetic fields

When the actuating magnetic field is spatially uniform, (*i.e.*, grad$\mathbf{B} = \mathbf{0}$), the magnetic body force terms vanish, significantly simplifying the governing equation. In general, the bending actuation of ferromagnetic soft continuum robots is driven by the magnetic body torque and further supported by the magnetic body force as the body deforms (Kim et al., 2019). Therefore, studying the response of the hard-magnetic elastica under uniform magnetic fields is of primary importance. Consider a hard-magnetic elastica lying on the x-axis with a uniform magnetization density along the body in the reference configuration, which is represented as $\mathbf{M} = M\mathbf{e}_x$ where M denotes the magnitude. When a uniform magnetic field

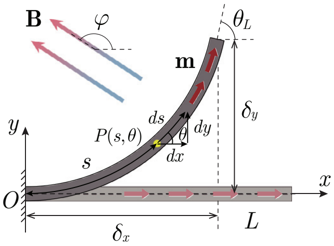

Fig. 4. Schematic of a hard-magnetic elastica under a uniform magnetic field **B**. The direction of the applied magnetic field is denoted as φ. The position of the tip is characterized by a Cartesian coordinate (δ_x, δ_y) and the rotation angle at the tip is denoted as θ_L.

is applied at an angle φ with respect to the reference configuration (*i.e.*, $\mathbf{B} = B\cos\varphi\mathbf{e}_x + B\sin\varphi\mathbf{e}_y$), as depicted in **Fig. 4**, the governing equation in Eq. (29) reduces to

$$\frac{EI}{A}\frac{d^2\theta}{ds^2} + MB\sin(\varphi - \theta) = 0. \tag{33}$$

With the help of chain rule, Eq. (32) can be expressed in the following integral form:

$$\int \frac{d^2\theta}{ds^2}\frac{d\theta}{ds}ds = -\int \frac{MBA}{EI}\sin(\varphi - \theta)d\theta, \tag{34}$$

which upon integration yields

$$\frac{1}{2}\left(\frac{d\theta}{ds}\right)^2 = -\frac{MBA}{EI}\cos(\varphi - \theta) + C. \tag{35}$$

The constant of integration C can be determined from the boundary condition that there is no internal bending moment at the free end, *i.e.*, $\theta'(L) = 0$ from Eqs. (16) and (18), which leads to

$$C = \frac{MBA}{EI}\cos(\varphi - \theta_L), \tag{36}$$

where θ_L denotes the angular displacement at the free end in the deformed configuration. Then, Eq. (35), along with Eq. (36), can be rearranged as

$$ds = \sqrt{\frac{EI}{2MBA}}\frac{d\theta}{\sqrt{\cos(\varphi - \theta_L) - \cos(\varphi - \theta)}}, \tag{37}$$

Integration of Eq. (37) leads to the expression for the total length of the elastica:

$$L = \sqrt{\frac{EI}{2MBA}}\int_0^{\theta_L}(\cos(\varphi - \theta_L) - \cos(\varphi - \theta))^{-1/2}d\theta = \sqrt{\frac{EI}{2MBA}}\Phi(\varphi, \theta_L), \tag{38}$$

where the nondimensional function $\Phi(\varphi, \theta_L)$ is defined as

$$\begin{aligned}\Phi(\varphi, \theta_L) &\equiv \int_0^{\theta_L}(\cos(\varphi - \theta_L) - \cos(\varphi - \theta))^{-1/2}d\theta \\ &= \frac{2}{\sqrt{\cos(\varphi - \theta_L) - 1}}\left[F\left(\frac{\varphi - \theta_L}{2}, \csc\left(\frac{\varphi - \theta_L}{2}\right)\right) - F\left(\frac{\varphi}{2}, \csc\left(\frac{\varphi - \theta_L}{2}\right)\right)\right],\end{aligned} \tag{39}$$

with the function F denoting the incomplete elliptic integral of the first kind defined as

$$F(\phi, k) \equiv \int_0^{\phi}\frac{d\theta}{\sqrt{1 - k^2\sin^2\theta}}. \tag{40}$$

Eq. (38) can then be rewritten as

$$\frac{MBAL^2}{EI} = \frac{1}{2}\Phi^2(\varphi, \theta_L), \tag{41}$$

which relates the dimensionless parameter $MBAL^2/EI$ with the angular displacement at the free end θ_L. The physical meaning of $MBAL^2/EI$ is the applied magnetic field strength normalized by the material properties M (magnetization) and E (modulus) and the geometrical factors A (cross-sectional area), L (length), and I (area moment of inertia).

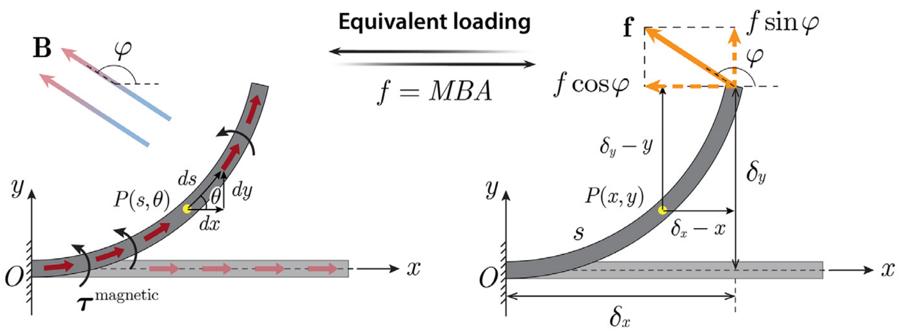

Fig. 5. Generalization of the distributed magnetic torque $\boldsymbol{\tau}^{\text{magnetic}}$ into an equivalent point force $\mathbf{f}$ acting on the free end of a hard-magnetic elastica. The equivalent point force has a magnitude of $f = MBA$ with a direction of φ relative to the reference configuration (x-axis). The two different loading conditions are equivalent, yielding the same deformed configuration of the elastica.

The kinematic relation in Eq. (31) in a differential form can be expressed as

$$\frac{d\mathbf{x}}{ds} = \cos\theta\,\mathbf{e}_x + \sin\theta\,\mathbf{e}_y, \tag{42}$$

which, along with Eq. (37), can also be expressed componentwise as

$$\begin{aligned} dx &= ds\cos\theta = \sqrt{\frac{EI}{2MBA}}\frac{\cos\theta\, d\theta}{\sqrt{\cos(\varphi-\theta_L)-\cos(\varphi-\theta)}}, \\ dy &= ds\sin\theta = \sqrt{\frac{EI}{2MBA}}\frac{\sin\theta\, d\theta}{\sqrt{\cos(\varphi-\theta_L)-\cos(\varphi-\theta)}}. \end{aligned} \tag{43}$$

Then, the Cartesian coordinates of the free end in the currnet configuration can be expressed as

$$\delta_x = \sqrt{\frac{EI}{2MBA}}X(\varphi,\theta_L) \text{ and } \delta_y = \sqrt{\frac{EI}{2MBA}}Y(\varphi,\theta_L), \tag{44}$$

where the functions $X(\varphi,\theta_L)$ and $Y(\varphi,\theta_L)$ are defined as

$$\begin{aligned} X(\varphi,\theta_L) &= \int_0^{\theta_L}\cos\theta\,(\cos(\varphi-\theta_L)-\cos(\varphi-\theta))^{-1/2}d\theta, \\ Y(\varphi,\theta_L) &= \int_0^{\theta_L}\sin\theta\,(\cos(\varphi-\theta_L)-\cos(\varphi-\theta))^{-1/2}d\theta. \end{aligned} \tag{45}$$

When normalized by the total length L, the free-end coordinates in Eq. (44) can be expressed as

$$\frac{\delta_x}{L} = \frac{X(\varphi,\theta_L)}{\Phi(\varphi,\theta_L)} \text{ and } \frac{\delta_y}{L} = \frac{Y(\varphi,\theta_L)}{\Phi(\varphi,\theta_L)}. \tag{46}$$

2.4. Equivalent point force at the free end

Consider a case in which a force denoted by a vector $\mathbf{f}$ is acting on the free end of the elastica in equilibrium in the deformed configuration, in the absence of the influence of external magnetic fields (*i.e.*, no magnetic body torque and force), as illustrated in Fig. 5**b**. The force $\mathbf{f}$ is being applied to the free end at an angle φ relative to the reference configuration (*i.e.*,$\mathbf{f} = f\cos\varphi\mathbf{e}_x + f\sin\varphi\mathbf{e}_y$). Referring to the free body diagram in Fig. 5**b**, we can set the following bending moment balance at the point $P(x, y)$

$$[\mathbf{M}_{\mathrm{b}} + \mathbf{r}\times\mathbf{f}]_z = -M_{\mathrm{b}}(x,y) - f\cos\varphi(\delta_y - y) + f\sin\varphi(\delta_x - \mathrm{x}) = 0. \tag{47}$$

Note that the horizontal component $f\cos\varphi$ depicted in Fig. 5**b** is negative when $\varphi > 90^\circ$. Then, from the moment-curvature relation in Eq. (18), we obtain

$$M_{\mathrm{b}}(x,y) = EI\frac{d\theta}{ds} = -f\cos\varphi(\delta_y - y) + f\sin\varphi(\delta_x - x). \tag{48}$$

Taking the derivative of Eq. (48) with respect to the arc length s and applying the differential kinematic relations in Eq. (42) leads to

$$EI\frac{d^2\theta}{ds^2} = f\cos\varphi\frac{dy}{ds} - f\sin\varphi\frac{dx}{ds} = f\cos\varphi\sin\theta - f\sin\varphi\cos\theta = -f\sin(\varphi-\theta). \tag{49}$$

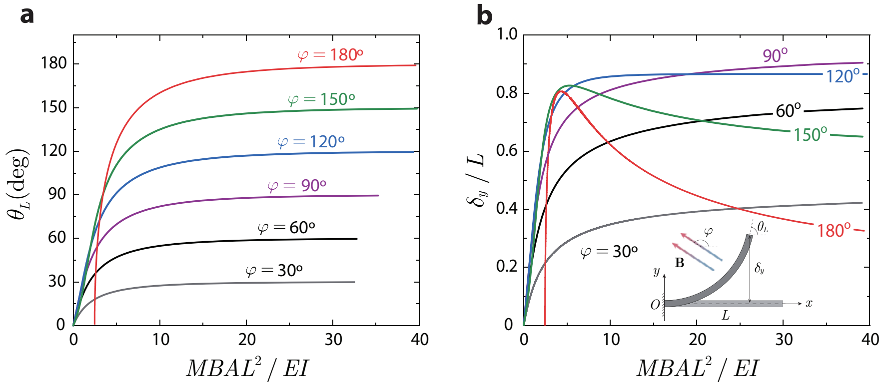

Fig. 6. Free-end location of the deflected elastica plotted against the normalized magnetic field strength $MBAL^2/EI$ with various angles φ: **(a)** angular displacement θ_L; **(b)** normalized tip deflection δ_y/L.

Comparing Eq. (49) with the governing equation obtained under the uniform magnetic field in Eq. (33), we notice that the force acting on the free end is equivalent to

$$f = MBA. \tag{50}$$

Here, both the uniform magnetic field **B** and the equivalent force **f** at the free end are applied to the elastica at an angle φ relative to the reference configuration. It is also worth noting that the two scenarios share the same boundary conditions: $\theta(0) = 0$ and $\theta'(L) = 0$. Treatment of the effect of distributed magnetic body torques developed under a uniform magnetic field as an equivalent force acting at the free end tip of the hard-magnetic elastica provides ease of calculation in the buckling analysis for hard-magnetic elastica under an antiparallel magnetic field (*i.e.*, $\varphi = 180^\circ$), as shown in Section **3.3**.

3. Results and validation

3.1. Deflection under uniform magnetic fields

We can solve Eq. (41) for the free-end angular displacement θ_L, with given material properties (M and E) and geometry (A, L, and I) under prescribed magnetic field strength (B) and direction (φ), which is presented in **Fig. 6a**. The free-end angle θ_L increases monotonically as the applied field strength increases and eventually approaches φ as the elastica becomes more aligned with the applied actuating field. From Eqs. (45) and (46), we also obtain the free-end location (normalized by the length L) of the deflected elastica with respect to the fixed end, as plotted in **Fig. 6b** against the normalized magnetic field $MBAL^2/EI$ applied at different angles φ relative to the reference configuration of the elastica. When $\varphi \leq 90^\circ$, the normalized free-end deflection δ_y/L increases monotonically and then becomes saturated. When $\varphi > 90^\circ$, however, the normalized deflection δ_y/L initially increases and then drops after reaching its peak as the elastica further deflects with the free-end angle θ_L being greater than 90°.

To validate the developed theory of hard-magnetic elastica, we compare our model-based prediction with finite element simulation and experimental results previously reported by Zhao et al. (2019) for two representative cases when i) $\varphi = 90^\circ$ (under perpendicular magnetic fields) and ii) $\varphi = 180^\circ$ (under antiparallel magnetic fields). In their simulations and experiments, rectangular beams made of hard-magnetic soft materials, in which the area moment of inertia was defined as $I = WC^3/12$. For hard-magnetic elastica with a rectangular cross-section with width W and height C, Eq. (41) can be expressed as

$$\frac{MB}{G}\left(\frac{L}{C}\right)^2 = \frac{1}{8}\Phi^2(\varphi, \theta_L), \tag{51}$$

where G denotes the shear modulus of the constituent material of the hard-magnetic elastica. We consider the material incompressible, in which Young's modulus is expressed as $E \simeq 3G$, as typical hyperelastic solids are often assumed to be incompressible with the shear modulus far greater than the bulk modulus. The hard-magnetic soft materials for the experimental validation (Zhao et al., 2019) were prepared by mixing NdFeB microparticles (**Fig. 2c**, average diameter ~5 μm) with PDMS (Sylgard 184). The mixture was cured at 120 °C for 1h and then magnetized along the axis direction by a strong impulse magnetic fields (~2.7 T) generated by an impulse magnetizer. The measured shear modulus and magnetization density values for hard-magnetic soft materials were reported as $G = 303$ kPa and $M = 144$ kA/m, respectively. Note that, as implied by Eq. (51), the length-to-thickness ratio L/C greatly affects how much the elastica would deflect under the same normalized field strength.

3.2. Under perpendicular magnetic fields ($\varphi = 90^\circ$)

When $\varphi = \pi/2$, Eq. (39) can be expressed as

$$\Phi(\varphi = \pi/2, \theta_L) = \frac{2}{\sqrt{\sin\theta_L - 1}}\left[F\left(\frac{\pi/2 - \theta_L}{2}, \sqrt{\frac{2}{1 - \sin\theta_L}}\right) - F\left(\frac{\pi}{4}, \sqrt{\frac{2}{1 - \sin\theta_L}}\right)\right], \tag{52}$$

while Eq. (45) can be expressed as

$$\begin{aligned} X(\varphi = \pi/2, \theta_L) &= 2\sqrt{\sin\theta_L}, \\ Y(\varphi = \pi/2, \theta_L) &= \frac{2\sin\theta_L}{\sqrt{\sin\theta_L - 1}}\left[F\left(\frac{\pi/2 - \theta_L}{2}, \sqrt{\frac{2}{1 - \sin\theta_L}}\right) - F\left(\frac{\pi}{4}, \sqrt{\frac{2}{1 - \sin\theta_L}}\right)\right] \\ &\quad -2\sqrt{\sin\theta_L - 1}\left[E\left(\frac{\pi/2 - \theta_L}{2}, \sqrt{\frac{2}{1 - \sin\theta_L}}\right) - E\left(\frac{\pi}{4}, \sqrt{\frac{2}{1 - \sin\theta_L}}\right)\right], \end{aligned} \tag{53}$$

with the function E denoting the incomplete elliptic integral of the second kind defined as

$$E(\phi, k) \equiv \int_0^\phi \sqrt{1 - k^2\sin^2\theta}\,d\theta \tag{54}$$

Then, by solving Eq. (51) for θ_L, along with Eq. (52) when $\varphi = \pi/2$, we can predict the free-end angular displacement as a function of the normalized magnetic field MB/G, as plotted in **Fig. 7a**. Also, from Eq. (46), along with Eqs. (52) and (53) for $\varphi = \pi/2$, we can also find the normalized free-end deflection δ_y/L as plotted against the normalized field MB/G in **Fig. 7b**. Finite element simulation (dashed lines) and experimental (square dots) results reported by Zhao et al. (2019) are also presented in **Fig. 7a** and **b**, for comparison, for different length-to-thickness ratios: $L/C = 10, 17.5, 20.5, 41$. For both measures, our model-based prediction is in good agreement with the simulation and experimental results. The slight gap between our theory and FEM/experiments may be attributed to the assumption of Euler-Bernoulli relation which often brings discrepancy especially for less slender beams with relatively small length-to-thickness ratios.

As shown in **Fig. 7**, our developed model captures the large deflection of hard-magnetic elastica particularly well for slender beams with high L/C. The relatively greater deviation for less slender beams (*i.e.*, when $L/C = 10$) may be attributed to the fact that our elastica theory is based on the assumption that the geometry of interest is slender enough to ignore transverse shearing while focusing on the centerline curve only, as described earlier. Nonetheless, there is still some deviation between our model-based prediction and the finite element simulation as shown in **Fig. 7a** and **b**, even for slender beams. This may be attributed to the fact that our theoretical formulation, for ease of calculation, is based on the quadratic form of the bending energy in Eq. (17), and consequently the Euler- Bernoulli relation in Eq. (18), which assumes a linear stress profile across the cross-sectional area.

Another underlying assumption in our theory is the centerline inextensibility discussed in **Section 2.2**. Hard-magnetic soft materials can undergo homogeneous deformation when subjected to a uniform magnetic field applied in parallel with the magnetization direction. In the case presented by Zhao et al. (2019), the uniaxial stretch λ can be expressed as

$$\lambda - \frac{1}{\lambda^2} = \frac{MB}{G}. \tag{55}$$

When the normalized field strength is high enough to make the curves saturated in **Fig. 7a** and **b**, *i.e.*, $MB/G = 0.02$, the stretch value is calculated as $\lambda = 1.0067$, which means that the beam made of hard-magnetic soft materials elongates by only 0.67% of the original length. This negligible contribution of homogeneous uniaxial deformation justifies the underlying assumption of centerline inextensibility we postulated when developing our theory for hard-magnetic elastica.

When overlaying our results on top of the simulation and experimental results for comparison, overall, we can observe good agreement with previously reported data, and hence conclude that our model provides a good quantitative prediction of the behavior of hard-magnetic elastica. In **Fig. 7a** and **b**, the applied magnetic field strength ranges from 0 to 50 mT, which corresponds to the normalized magnetic field strength MB/G ranging from 0 to 0.019. In **Fig. 7c**, the applied field strength is 25 mT, which corresponds to $MB/G = 0.0094$. Note that the current theory assumes that the remanent magnetization is independent of the actuation field and that the actuation field is unperturbed by the presence of the hard-magnetic elastica, which may also contribute to the discrepancy.

3.3. Under antiparallel magnetic fields ($\varphi = 180^\circ$)

When $\varphi = \pi$, Eq. (39) can be expressed as

$$\Phi(\varphi = \pi, \theta_L) = \frac{2}{\sqrt{1 - \cos\theta_L}} F\left(\frac{\theta_L}{2}, \csc\left(\frac{\theta_L}{2}\right)\right), \tag{56}$$

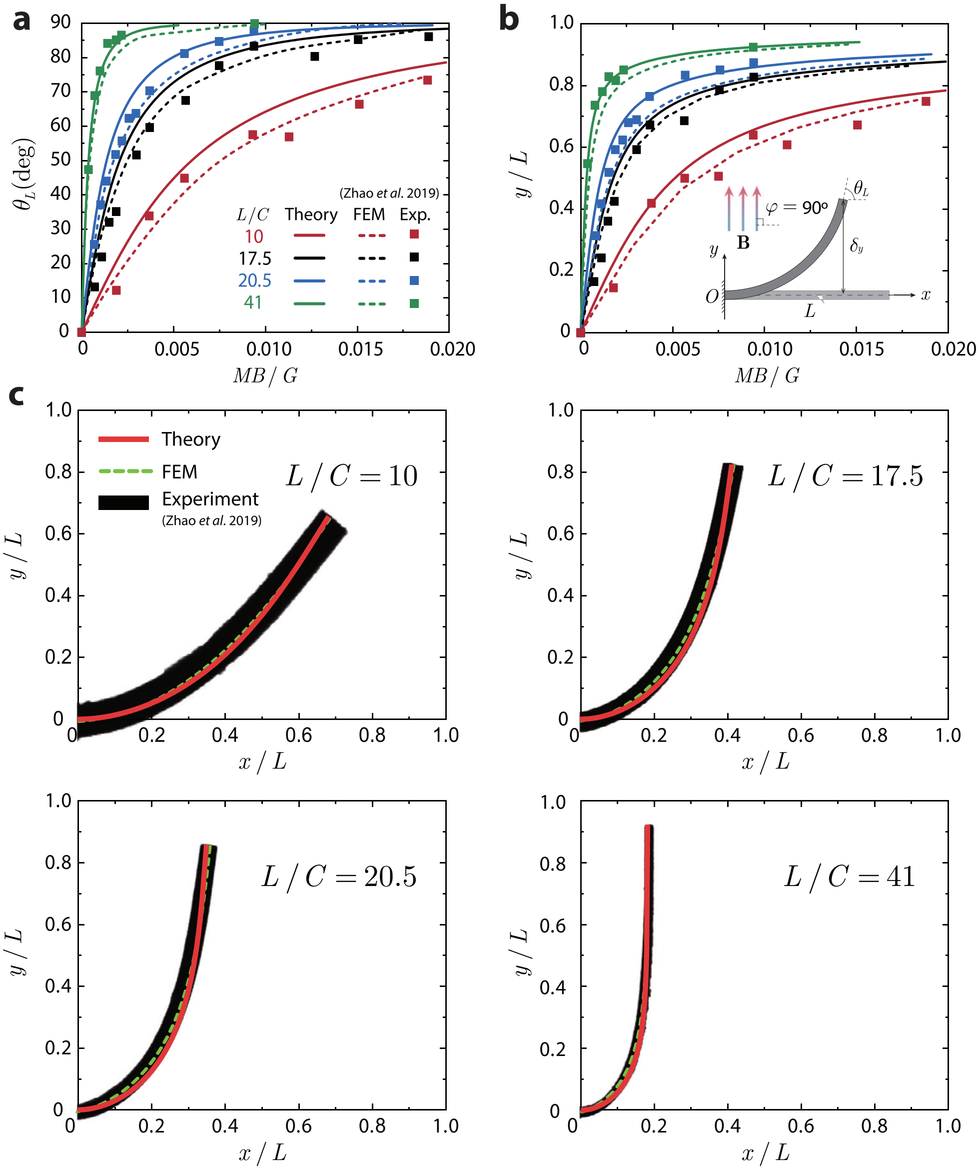

Fig. 7. Comparison of our analytical predictions from the developed hard-magnetic elastica theory with finite element simulation (FEM) and experimental results (Zhao et al., 2019) under a perpendicular magnetic field ($\varphi = 90^\circ$). **(a)-(b)** The tip rotation angle θ_L and normalized tip deflection δ_y/L plotted each as a function of the normalized magnetic flux density MB/G. The inset shows the schematic of the hard-magnetic elastica under consideration. **(c)** Deformed elastica with different length-to-thickness ratios $L/C = 10, 17.5, 20.5, 41$. The black shapes are experimental observations, and the dashed lines and red curves represent the centerlines of the deformed beam predicted from FEM simulations and analytical solutions. The applied magnetic field strength ranges from 0 to 50 mT, which corresponds to the normalized magnetic field strength MB/G ranging from 0 to 0.0019.

while Eq. (45) can be expressed as

$$\begin{aligned}
X(\varphi=\pi,\theta_L) &= \frac{2}{\sqrt{1-\cos\theta_L}}\left[\cos\theta_L F\left(\frac{\theta_L}{2},\csc\left(\frac{\theta_L}{2}\right)\right)+(1-\cos\theta_L)E\left(\frac{\theta_L}{2},\csc\left(\frac{\theta_L}{2}\right)\right)\right],\\
Y(\varphi=\pi,\theta_L) &= 2\sqrt{1-\cos\theta_L}.
\end{aligned}\tag{57}$$

When the deflection is small enough that the tip rotation approaches to zero, *i.e.*, $\theta_L \to 0$, Eq. (56) yields $\lim_{\theta_L\to 0}\Phi(\pi,\theta_L) = \pi/\sqrt{2}$, and then Eq. (41) becomes

$$MB_{\mathrm{cr}}A = \frac{\pi^2 EI}{4L^2} = P_{\mathrm{cr}},\tag{58}$$

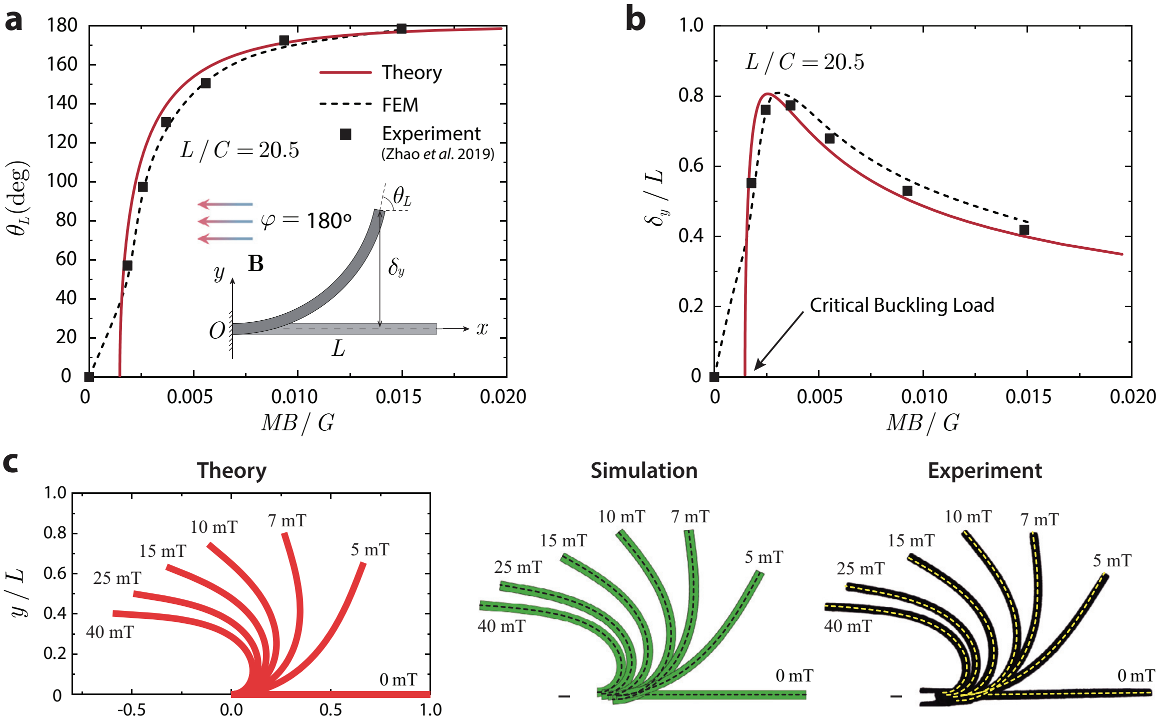

Fig. 8. Comparison of our analytical predictions from the developed hard-magnetic elastica theory with the finite element simulations (FEM) and experimental results (Zhao et al., 2019) under an antiparallel magnetic field ($\varphi = 180^\circ$). **(a)-(b)** The tip rotation angle θ_L and normalized tip deflection δ_y/L as a function of the normalized magnetic field MB/G for a beam with a length-to-thickness ratio $L/C = 20.5$. The critical buckling load is $MB_{\mathrm{cr}}/G \simeq 0.00147$. **(c)** Deformed profile of the beam with a length-to-thickness ratio $L/C = 20.5$ under different magnetic field strengths $B = 5, 7, 10, 15, 25, 40$ mT. The black areas are experimental observations, and the dashed lines and red curves represent the centerlines of the deformed beams predicted from FEM simulations and analytical solutions.

where P_{cr} is the critical compressive load beyond which the column (with length L, Young's modulus E, and area moment of inertia I) buckles when applied along the axial direction. We define the applied magnetic field that satisfies Eq. (58) as the critical field strength B_{cr}. Interestingly, Eq. (58) implies that, when $\varphi = \pi$, the equivalent point force $f = MBA$ is applied in such a way that compresses the column (*i.e.*, in the direction of the applied magnetic field) and hence can cause buckling when the applied field strength exceeds the critical field strength (*i.e.*, $B \geq B_{\mathrm{cr}}$). This analysis further corroborates our interpretation of the magnetoelastic bending actuation as the consequence of the equivalent point force at the free end given in Eq. (50).

For a rectangular beam, the critical field strength can be expressed from Eq. (51) as

$$\frac{MB_{\mathrm{cr}}}{G} = \frac{\pi^2 C^2}{16L^2}. \tag{59}$$

By solving Eq. (51) for θ_L, along with Eq. (56) when $\varphi = \pi$, we can predict the free-end angular displacement as a function of the normalized magnetic field MB/G, as plotted in **Fig. 8a**. Also, from Eq. (46), along with Eqs. (56) and (57) for $\varphi = \pi$, we can also find the normalized free-end deflection δ_y/L as plotted against the normalized field MB/G in **Fig. 8b**. Finite element simulation (dashed lines) and experimental (square dots) results reported by Zhao et al. (2019) are also presented in **Fig. 8a** and **b**, for comparison, for a specific length-to-thickness ratio: $L/C = 20.5$. For both measures, our model-based prediction shows good agreement with previously reported data by Zhao et al. (2019) except for the fact that their finite element simulation did not anticipate the buckling instability predicted by our theoretical model from Eq. (59) above.

Plugging the material properties ($G = 303$ kPa and $M = 144$ kA/m) and dimension ($L/C = 20.5$) into Eq. (59), we can calculate the critical field strength to be $MB_{\mathrm{cr}}/G \simeq 0.00147$, which corresponds to 3.9 mT for the given material and geometry. The inability to capture such buckling instability with finite element simulation may be attributed to the following reasons. To simulate the magnetoelastic bending of hard-magnetic elastica subjected to an antiparallel magnetic field in finite element environment, there should be a slight misalignment (Δ) between **M** and **B** (*i.e.*, $\varphi = \pi - \Delta$), because nothing but homogeneous compression would happen under perfectly antiparallel field unless the beam has geometric imperfections or perturbations. In other words, the use of the slightly inclined actuating field to compensate for the absence of geometric imperfections would likely have prevented Zhao et al., 2019 from observing the buckling instability from their finite element simulation.

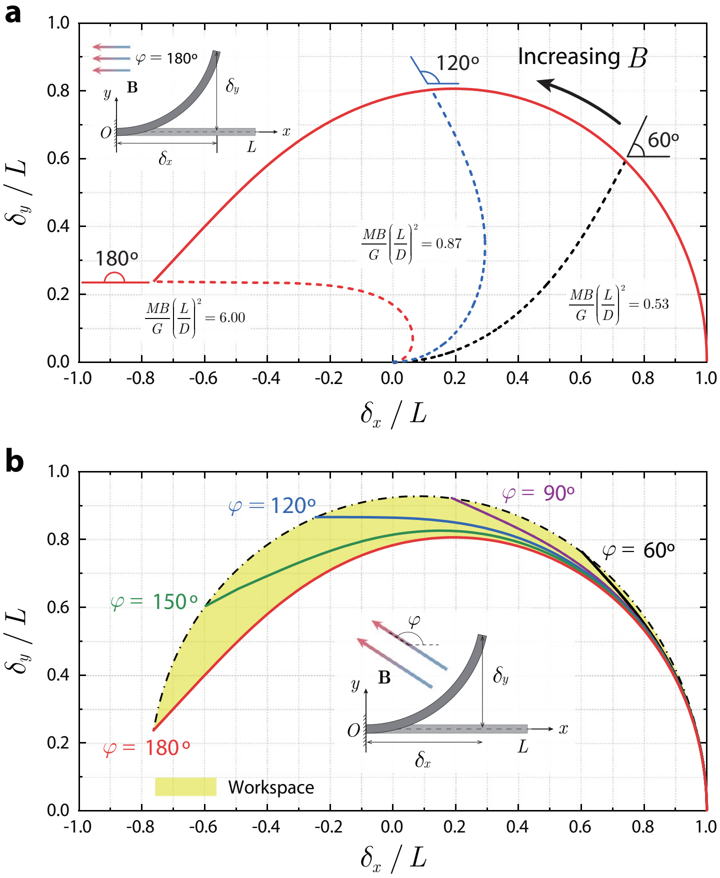

Fig. 9. (**a**) The trajectory of the robot's end effector on a dimensionless plane normalized by the length L under an antiparallel magnetic field applied at $\varphi = 180°$. By tuning the applied magnetic field strength, the continuum robot can be steered to various configurations. The dashed curves represent the configurations under normalized magnetic field strengths $(MB/G)/(L/D)^2 = 0.53, 0.87, 6.00$. (**b**) The workspace reachable by the robot's end effector is highlighted by the shaded area as the control parameters B and φ vary simultaneously. The solid curves represent the trajectory of the robot's end effector under various magnetic fields applied from different directions $\varphi = 60°, 90°, 120°, 150°, 180°$.

Fig. 8**c** visually and directly compares the degrees of bending of the beam theoretically predicted (left), simulated (middle), and experimentally observed (right) at a set of prescribed field strengths. From their close agreement, we conclude that our developed model is capable of quantitatively and accurately predicting the large magnetoelastic deflection of hard-magnetic elastica under uniform magnetic fields. It should be noted that, for general elastica problems, the slender rod may interact with itself under extreme bending. In those scenarios, the self-interaction of the elastica needs to be considered accordingly. In the current study, we have not observed significant mechanical or magnetic self-interaction of the hard-magnetic elastica under magnetic actuation and thus have not taken such self-interaction into account, which may be explored in future studies.

4. Applications

4.1. Workspace of ferromagnetic soft continuum robots

In the context of ferromagnetic soft continuum robots which were discussed earlier in Fig. 1, it is important to know the workspace reachable by the robot's end effector, *i.e.*, the free-end of the elastica. When the length L is fixed, the deflection of the continuum robot can be controlled by varying the applied field strength (B) and direction (φ), as shown in Fig. 9. Let us first take the scenario when $\varphi = 180°$ as an example. The trajectory of the robot's end effector (δ_x, δ_y) is plotted on a dimensionless plane (normalized by L) as the solid red curve in Fig. 9**a**. Three representative magnetic fields $(MB/G)/(L/D)^2 = 0.53, 0.87, 6.00$, in a normalized form, are selected, which correspond to three tip rotation angles $\theta_L = 60°, 120°, 180°$, at which the deformed configurations of the robot are shown by the dashed curves in Fig. 9**a**. Apparently, a stronger field induces a higher degree of bending of the robot.

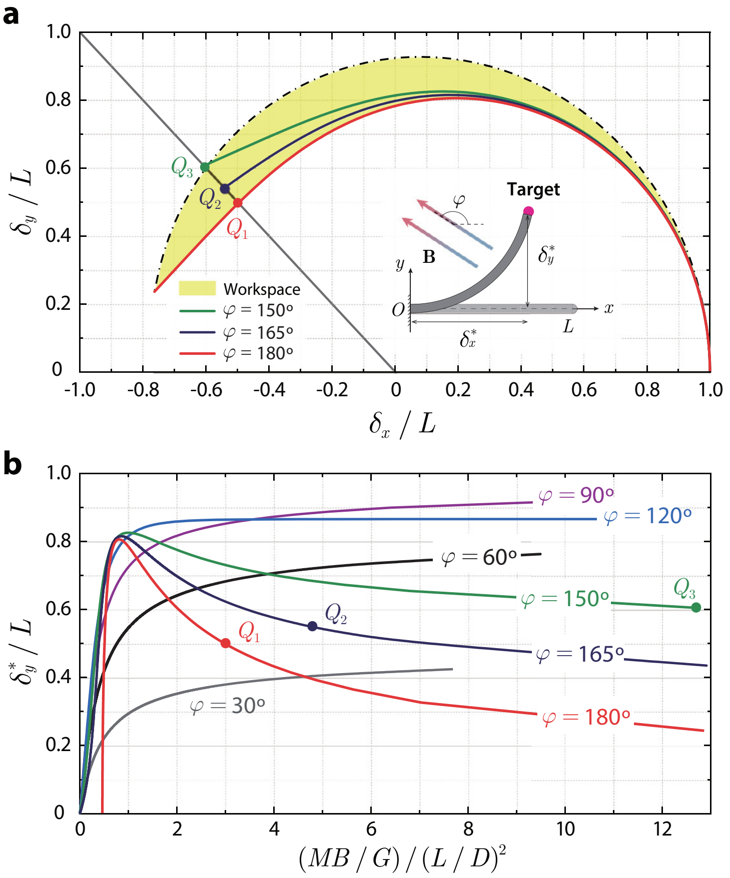

Fig. 10. The control variables (φ, B, L) required for the robot's end effector to reach a target location (δ_x^*, δ_y^*) can be determined from the workspace analysis. **(a)** The required magnetic field direction φ can be identified from the intersection between the straight line with a slope of δ_y^*/δ_x^* and the tip trajectory in the workspace. **(b)** Target deflection δ_y^*/L plotted against the normalized magnetic field input $(MB/G)/(L/D)^2$.

In addition, the trajectory of the robot's end effector varies when the magnetic field changes its direction, as shown by the solid curves ($\varphi = 60^\circ, 90^\circ, 120^\circ, 150^\circ, 180^\circ$) in Fig. 9**b**. Integrating all the trajectories corresponding to different directions of the applied magnetic fields visualizes the workspace sweeped by the robot's end effector (Fig. 9**b**). Any point on the workspace can be reached by the robot's end effector under an applied magnetic field with specific direction φ and field strength B, from which we can solve an inverse problem, as discussed in the following section.

4.2. Procedure to reach target locations

Solving an inverse problem means to find control inputs required for a ferromagnetic soft continuum robot to steer and place its end-effector to a tartget location, which is denoted by a specific point (δ_x^*, δ_y^*) in the space. We first draw a straight line with a slope of δ_y^*/δ_x^* from the origin of the workspace diagram in Fig. 10**a**. If this line has no intersection with the workspace (*i.e.*, shaded area), the target location cannot be reached by the robot's end effector. If the line intersects with the workspace, any point on the intersecting segment of the line can be reached by the robot's end-effector, provided that an appropriate set of control variables (φ, B, L) is chosen. For example, let us consider a target point that can be prescribed by $\delta_y^*/\delta_x^* = -1$. A straight line with a slope of -1 can be drawn from the origin of the workspace diagram in Fig. 10**a**. The lower and upper boundaries of the reachable domain are labeled as Q_1 with $\delta_y^*/\delta_x^* = (-0.5, 0.5)$ and Q_3 with $\delta_y^*/\delta_x^* = (-0.6, 0.6)$, which are the intersections between the drawn line and the lower and upper envelopes of the workspace, respectively. Because Q_1 and Q_3 fall on the robot's trajectories when $\varphi = 180^\circ$ and $\varphi = 150^\circ$, the required magentic field directions to reach Q_1 and Q_3 can be found as $\varphi = 180^\circ$and $\varphi = 150^\circ$, respectively. As another example, the actuating magnetic field should be applied at $\varphi = 165^\circ$ for the robot's end-effector to reach a target located at $(\delta_x^*, \delta_y^*) = (-0.55, 0.55)$, which is marked as Q_2 in **Fig. 10a**.

After the required magnetic field direction φ is selected, the length of the robot L required to reach the target location can be calculated from Fig. 10**a**. For example, for $\varphi = 180^\circ$ (*i.e.*, Q_1), we have $(\delta_x^*, \delta_y^*) = (-0.5, 0.5)$ from Fig. 10**a**. Thereafter, the corresponding magnetic field strength B to reach the target location can be determined from Fig. 10**b,** in which δ_y^*/L

is plotted as a function of normalized magnetic field strength $(MB/G)/(L/D)^2$ for various φ. We know from **Fig. 10b** that input mangetic fields of $(MB/G)(L/D)^2 = 2.96, 4.71, 12.71$ are needed to reach the target locations Q_1, Q_2, Q_3, respectively. Furthermore, it can be seen that a selection of field direction closer to the upper envelope of the workspace (*i.e,* Q_3) with a greater deviation from the antiparallel configuration (*i.e.,* Q_1) requires a stronger magnetic field to reach the target.

4.3. Bending actuation under spatially non-uniform magnetic fields

For ease of calculation and simplicity, we present analytical solutions and relevant analyses for the hard-magnetic elastica under spatially uniform magnetic fields. In the presence of a spatial gradient (*e.g.,* when actuating continuum robots with a single permanent magnet as demonstrated by Kim et al., 2019), the magnetic body force, as well as the magnetic body torque, contributes to the bending actuation of the ferromagnetic soft continuum robot (**Fig. 3a**), as predicted from Eq. (14). As the equation implies, the magnetic body force varies with the deformation gradient **F**, or more specifically, with the robot's configuration relative to the applied magnetic field. In the reference configuration, in which the external field is being applied perpendicularly to the magnetization vector (**Fig. 3a**), the magnetic body force is almost negligible as predicted from Eq. (14), and hence the magnetoelastic bending actuation is driven mostly by the magnetic body torque. The magnetic body force increases, whereas the magnetic body torque decreases, as the robot's body deforms and its magnetization vector becomes more aligned with the applied field. In other words, the bending actuation, which is initiated and driven by the magnetic body torque, is facilitated and further supported or stabilized by the magnetic body force as the robot's body deforms (Kim et al., 2019). We can, therefore, conclude that utilizing spatial gradients to exploit magnetic body forces can be a good strategy to more effectively control the magnetic steering of ferromagnetic soft continuum robots.

5. Conclusions

In this paper, we presented a nonlinear theory for hard-magnetic elastica, which enables accurate prediction of the large magnetoelastic deflections of slender beams with intrinsic magnetic dipoles under the influence of external magnetic fields. We summarized a continuum-level description for analyzing hard-magnetic soft materials based on elastic and magnetic Cauchy stresses. Then, by applying constraints specific to the planar motion of a slender beam, we derived the governing equations, from which we obtained explicit analytical solutions for the hard-magnetic elastica under spatially uniform magnetic fields. We validated our developed theory for hard-magnetic elastica by comparing the obtained solutions with previously reported finite element simulation and experimental data. The validated model was employed to analyze the workspace of ferromagnetic soft continuum robots for their practical applications, which also provided simple but effective strategies to determine control variables required to reach target locations with the robot's end effector. Our developed theoretical model enables easier and faster quantitative analysis of hard-magnetic elastica than computation-expensive finite element simulation, and therefore suggests applications in the design and control of the emerging class of ferromagnetic soft continuum robots.

Authors' contribution

Liu Wang: Conceptualization, Methodology, Formal analysis, Investigation, Writing - original draft, Writing - review & editing. **Yoonho Kim**: Conceptualization, Methodology, Formal analysis Investigation, Writing - original draft, Writing - review & editing. **Chuan Fei Guo**: Writing - Writing - review & editing, Supervision, Funding acquisition; **Xuanhe Zhao**: Conceptualization, Methodology, Writing - original draft, Writing - review & editing, Supervision, Funding acquisition.

Declaration of Competing Interest

The authors declare that they have no known competing financial interests or personal relationships that could have appeared to influence the work reported in this paper.

Acknowledgement

This work is supported by the "Science Technology the Shenzhen Sci-Tech Fund" (no. KYTDPT20181011104007), and the "Guangdong Innovative and Entrepreneurial Research Team Program" under Contract no. 2016ZT06G587. L. Wang acknowledges the support from Centers for Mechanical Engineering Research and Education at MIT and SUSTech. Y. Kim acknowledges the financial support through a scholarship from ILJU Academy and Culture Foundation.

Appendix A

The derivative of a rotation tensor can be expressed as the skew-symmetric matrix of the unit axis vector multiplied with the rotation itself:

$$\frac{\partial \mathbf{R}_z(\theta)}{\partial \theta} = \mathbf{S}(\mathbf{e}_z)\mathbf{R}_z(\theta), \tag{60}$$

where the skew-symmetric matrix of a vector $\mathbf{u}$ is defined as

$$\mathbf{S}(\mathbf{u}) = u_z(\mathbf{e}_y \otimes \mathbf{e}_x - \mathbf{e}_x \otimes \mathbf{e}_y) + u_y(\mathbf{e}_x \otimes \mathbf{e}_z - \mathbf{e}_z \otimes \mathbf{e}_x) + u_x(\mathbf{e}_z \otimes \mathbf{e}_y - \mathbf{e}_y \otimes \mathbf{e}_z). \tag{61}$$

When operating on a vector $\mathbf{v}$, the skew-symmetric tensor $\mathbf{S}(\mathbf{u})$ produces the cross product of the two vectors: $\mathbf{S}(\mathbf{u})\mathbf{v} = \mathbf{u} \times \mathbf{v}$, which transforms the first term on the right-hand side of Eq. (23) into

$$\frac{\partial \mathbf{R}}{\partial \theta}\mathbf{M} \cdot \mathbf{B} = (\mathbf{e}_z \times \mathbf{RM}) \cdot \mathbf{B} = \mathbf{e}_z \cdot (\mathbf{RM} \times \mathbf{B}) = [\mathbf{RM} \times \mathbf{B}]_z, \tag{62}$$

as given in Eq. (26).

Reference

Bretl, T., McCarthy, Z., 2013. Quasi-static manipulation of a Kirchhoff elastic rod based on a geometric analysis of equilibrium configurations. Int. J. Robot. Res. 33, 48–68.

Camarillo, D.B., Carlson, C.R., Salisbury, J.K., 2009. Configuration tracking for continuum manipulators with coupled tendon drive. IEEE Trans. Rob. 25, 798–808.

Ciambella, J., Favata, A., Tomassetti, G., 2018. A nonlinear theory for fibre-reinforced magneto-elastic rods. Proc. Math. Phys. Eng. Sci. 474, 20170703.

Clogenson, H.C.M., Dankelman, J., van den Dobbelsteen, J.J., 2014. Steerable guidewire for magnetic resonance guided endovascular interventions. J. Med. Devices 8, 021002.

Dalvand, M.M., Nahavandi, S., Howe, R.D., 2018. An analytical loading model for $ n $-tendon continuum robots. IEEE Trans. Rob. 34, 1215–1225.

Danas, K., Kankanala, S.V., Triantafyllidis, N., 2012. Experiments and modeling of iron-particle-filled magnetorheological elastomers. J. Mech. Phys. Solids. 60, 120–138.

de Payrebrune, K.M., O'Reilly, O.M., 2016. On constitutive relations for a rod-based model of a pneu-net bending actuator. Extreme Mech. Lett. 8, 38–46.

Diller, E., Zhuang, J., Zhan Lum, G., Edwards, M.R., Sitti, M., 2014. Continuously distributed magnetization profile for millimeter-scale elastomeric undulatory swimming. Appl. Phys. Lett. 104, 174101.

Dorfmann, A., Ogden, R.W., 2003. Magnetoelastic modelling of elastomers. Eur. J. Mech.-A/Solids 22, 495–507.

Dorfmann, A., Ogden, R.W., 2004. Nonlinear magnetoelastic deformations of elastomers. Acta Mech. 167, 13–28.

Dorfmann, L., Ogden, R.W., 2014. Nonlinear Theory of Electroelastic and Magnetoelastic Interactions. Springer.

Edelmann, J., Petruska, A.J., Nelson, B.J., 2017. Magnetic control of continuum devices. Int. J. Robot. Res. 36, 68–85.

Fu, Y., Liu, H., Huang, W., Wang, S., Liang, Z., 2009. Steerable catheters in minimally invasive vascular surgery. Int. J. Med. Robot. Comput. Assist. Surg. 5, 381–391.

Gerbal, F., Wang, Y., Lyonnet, F., Bacri, J.-C., Hocquet, T., Devaud, M., 2015. A refined theory of magnetoelastic buckling matches experiments with ferromagnetic and superparamagnetic rods. Proc. Natl. Acad. Sci. 112, 7135.

Holzapfel, G.A., 2001. Nonlinear Solid Mechanics: a Continuum Approach for Engineering. Wiley.

Hu, W., Lum, G.Z., Mastrangeli, M., Sitti, M., 2018. Small-scale soft-bodied robot with multimodal locomotion. Nature 554, 81.

Jiang, F., Tian, S., Yu, W., 2016. Nonlinear modelling of axially deformable elastica based on hyperelasticity. 57th AIAA/ASCE/AHS/ASC Structures, Structural Dynamics, and Materials Conference, 1242.

Kim, Y., Parada, G.A., Liu, S., Zhao, X., 2019. Ferromagnetic soft continuum robots. Sci. Robot. 4, eaax7329.

Kim, Y., Yuk, H., Zhao, R., Chester, S.A., Zhao, X., 2018. Printing ferromagnetic domains for untethered fast-transforming soft materials. Nature 558, 274.

Kratchman, L.B., Bruns, T.L., Abbott, J.J., Webster, R.J., 2016. Guiding elastic rods with a robot-manipulated magnet for medical applications. IEEE Trans. Rob. 33, 227–233.

Lum, G.Z., Ye, Z., Dong, X., Marvi, H., Erin, O., Hu, W., Sitti, M., 2016. Shape-programmable magnetic soft matter. Proc. Natl. Acad. Sci. 113, E6007–E6015.

Menaker, S.A., Shah, S.S., Snelling, B.M., Sur, S., Starke, R.M., Peterson, E.C., 2018. Current applications and future perspectives of robotics in cerebrovascular and endovascular neurosurgery. J. Neurointerventional Surg. 10, 78–82.

O'Reilly, O.M., 2017. Modeling Nonlinear Problems in the Mechanics of Strings and Rods. Springer.

Pyrhönen, J., Ruoho, S., Nerg, J., Paju, M., Tuominen, S., Kankaanpää, H., Stern, R., Boglietti, A., Uzhegov, N., 2014. Hysteresis losses in sintered NdFeB permanent magnets in rotating electrical machines. IEEE Trans. Ind. Electron. 62, 857–865.

Ranzani, T., Gerboni, G., Cianchetti, M., Menciassi, A., 2015. A bioinspired soft manipulator for minimally invasive surgery. Bioinspiration Biomimetics 10.

Renda, F., Cianchetti, M., Giorelli, M., Arienti, A., Laschi, C., 2012. A 3D steady-state model of a tendon-driven continuum soft manipulator inspired by the octopus arm. Bioinspiration Biomimetics 7.

Robinson, G., Davies, J.B.C., 1999. Continuum robots - a state of the art. In: Proceedings 1999 IEEE International Conference on Robotics and Automation (Cat. No.99CH36288C), 2844, pp. 2849–2854.

Runciman, M., Darzi, A., Mylonas, G.P., 2019. Soft Robotics in minimally invasive surgery. Soft Robot..

Schmauch, M.M., Mishra, S.R., Evans, B.A., Velev, O.D., Tracy, J.B., 2017. Chained iron microparticles for directionally controlled actuation of soft robots. ACS Appl. Mater. Inter. 9, 11895–11901.

Shepherd, R.F., Ilievski, F., Choi, W., Morin, S.A., Stokes, A.A., Mazzeo, A.D., Chen, X., Wang, M., Whitesides, G.M., 2011. Multigait soft robot. PNAS 108, 20400–20403.

Singh, R.P., Onck, P.R., 2018. Magnetic field induced deformation and buckling of slender bodies. Int. J. Solids Struct. 143, 29–58.

Tunay, I., 2004. Modeling magnetic catheters in external fields. In: The 26th Annual International Conference of the IEEE Engineering in Medicine and Biology Society. IEEE, pp. 2006–2009.

Tunay, I., 2013. Spatial continuum models of rods undergoing large deformation and inflation. IEEE Trans. Rob. 29, 297–307.

Zhang, J., Diller, E., 2018. Untethered miniature soft robots: modeling and design of a millimeter-scale swimming magnetic sheet. Soft Robot. 5, 761–776.

Zhao, R., Kim, Y., Chester, S.A., Sharma, P., Zhao, X., 2019. Mechanics of hard-magnetic soft materials. J. Mech. Phys. Solids 124, 244–263.

Zhou, R., Wang, C., 2016. Microfluidic separation of magnetic particles with soft magnetic microstructures. Microfluid. Nanofluid. 20, 48.